ISSN 1027-4510, Journal of Surface Investigation. X-ray, Synchrotron and Neutron Techniques, 2016, Vol. 10, No. 2, pp. 282–291. © Pleiades Publishing, Ltd., 2016.
Original Russian Text © V.F. Pichugin, A.A. Pustovalova, M.E. Konishchev, I.A. Khlusov, N.M. Ivanova, Sun Zhilei, S.S. Gutor, 2016, published in Poverkhnost'. Rentgenovskie, Sinkhrotronnye i Neitronnye Issledovaniya, 2016, No. 3, pp. 19–29.

In-vitro Dissolution and Structural and Electrokinetic Characteristics of Titanium-Oxynitride Coatings Formed via Reactive Magnetron Sputtering

V. F. Pichugin[a]*, A. A. Pustovalova[a], M. E. Konishchev[a], I. A. Khlusov[a, b], N. M. Ivanova[a], Sun Zhilei[a], and S. S. Gutor[b]

[a] *Tomsk Polytechnic University, Tomsk, 634050 Russia*
[b] *Siberian State Medical University, Tomsk, 634050 Russia*
**e-mail: pichugin@tpu.ru*
Received August 10, 2015

Abstract—The results of investigation into the structure and in-vitro dissolution of titanium-oxynitride coatings deposited via reactive magnetron sputtering are presented. Data on the electrostatic and ζ surface potentials enable estimation of their contribution to adsorption processes and coating dissolution in vitro. Sample cultivation in a solution simulating the composition of the inorganic part of human blood plasma leads to surface mineralization, reduces the value and sign of the surface potential, and alters the surface wettability. The coating prevents the transition of iron ions into a solution and does not induce the calcification of an artificial surface.

Keywords: magnetron sputtering, titanium oxynitrides, ζ potential, dissolution, biocompatibility
DOI: 10.1134/S1027451016020166

INTRODUCTION

The biocompatibility of the surfaces of medical implants is an urgent problem of medical materials science. Such a problem is especially critical in vascular surgery and cardiosurgery because almost 10% of patients with implants suffer from repeated narrowing of the blood-vessel lumen near stents. To prevent adverse organism responses to vascular endoprostheses, biocompatible coatings are created on their surfaces [1–3].

Combined (TiON) films are promising coatings of coronary stents [4, 5]. Coatings based on titanium oxides and oxynitrides hamper thrombosis and fibrinogen deposition on stent surfaces [6, 7]. The biological properties of TiON films can be controlled with the help of their own structure and chemical composition. A special role is played by the oxygen–nitrogen ratio of the coatings. Their bioinertness is regulated by titanium and its oxides, while the nitrogen-oxide molecules of the coatings and/or their precursors determine their bioactive properties [8].

Such coatings with protective and bioactive potentials can be efficiently deposited via plasma techniques, in particular, magnetron sputtering [9, 10]. In accordance with film-growth modes, the prepared coatings can have different properties: from dielectric (titanium dioxide) to semiconducting (TiON) and conducting (TiN). When a film possesses dielectric properties, its surface is charged [11]. The interaction between an artificial surface and living tissue and blood depends heavily on the amount and sign of its charge.

In recent years, great attention has been paid to research into the electrokinetic characteristics of the "artificial surface–electrolyte" interaction [12–17]. First of all, this is related to the fact that, in the development of biomaterials, knowledge of the surface charge is of great importance. Moreover, interest in the study of interactions observed at the artificial-surface–electrolyte interface is associated with the creation of an electrokinetic analyzer [18, 19] which enables the fairly simple obtainment of electrokinetic potentials. The ζ-potential measurement method has found application in investigating the properties of different materials [13–15]. Changes in the ζ potential are used to determine the adsorption of proteins (albumins and fibrinogens) from blood plasma on a polymer surface [20]. The ζ potential of mica samples covered with latex particles was analyzed in [15], the authors of which determined the ζ potentials of a substrate and particles. It was concluded that the ζ-potential measurement method is an efficient tool for investigating colloids and bioparticles. In the case of thin titanium films, results demonstrating how the properties and value of their ζ potentials affect protein adsorption and cell proliferation are reported in [16]. The authors of [17] investigated the electrokinetic

characteristics of polysulfone membranes immersed in a sodium-chloride (NaCl) solution at different concentrations and pH values. The obtained data made it possible to determine the following membrane parameters: surface charge densities, Gibbs free energies, and adsorption-center densities on a surface.

A change in the ζ potential plays a decisive role in the aggregation of blood cells interacting with an artificial surface [21–23]. At the same time, the streaming potential of titanium-oxynitride films produced by means of the magnetron sputtering method and their ζ potential have never been investigated despite the fact that the given type of coatings is promising for medical applications. Moreover, such coatings are widely used to fabricate vascular endoprostheses (stents) [24–26].

In the context of the foregoing, this work presents the results of studying the structure and properties of titanium-oxynitride coatings deposited onto medical-steel samples via reactive medium-frequency magnetron sputtering, the data of research into the electrostatic and ζ surface potentials, and the estimates of their contribution to adsorption and coating dissolution processes in vitro.

MATERIALS AND INVESTIGATION METHODS

Titanium-oxynitride coatings were formed via reactive magnetron sputtering by means of a UVN-200MI medium-frequency magnetron sputtering setup (Tomsk Polytechnic University, Tomsk) [27]. Oxygen and nitrogen were mixed in different ratios, and their mixture was used as a plasma-forming and reactive gas. L316 stainless-steel samples were chosen as substrates onto which the coatings were deposited. The deposition process was carried out under the following conditions: the sputtered target material was titanium; the working-chamber pressure was 0.1 Pa; the power and current were, respectively, 1 kW and 3 A; the working-gas inflow rate was 5 mL/min; and the distance between the substrate and the magnetron was 100 mm. Titanium oxide (TiO_2) (sample group I) was sputtered in an O_2 atmosphere. Titanium oxynitrides were deposited at different ratios between N_2 and O_2 mass flow rates in the working environment: $p(O_2)/p(N_2) = 1/1$ (sample group II) and $p(O_2)/p(N_2) = 1/3$ (sample group III). The film-deposition modes were controlled via optical emission spectroscopy by means of an AvaSpec-3648 spectrometer with a wavelength range of 200–1000 nm [27]. Optical-spectrum lines were identified using the NIST atomic spectra database [28]. During the deposition process, the substrate temperature was 120°C. The synthesized-coating thicknesses were measured using an Ellips-1891 SAG ellipsometric complex at a fixed light-incidence angle of 70° and wavelengths of 250–1000 nm. The coating thicknesses were determined using developed air–TiO_2–substrate and air–TiON–substrate models.

Table 1. Characteristics of the coating samples under study (according to energy-dispersive analysis data), namely, the TiO_2 (sample group I), the O_2 atmosphere, the TiON, and the ratio between the O_2 and N_2 mass flow rates in the working atmosphere: $p(O_2)/p(N_2) = 1/1$ (sample group II) and $p(O_2)/p(N_2) = 1/3$ (sample group III)

Sample	N, at %	O, at %	Ti, at %
TiO_2 (I)	–	84.41	15.59
TiON (II)	5.71	80.27	14.02
TiON (III)	6.16	80.01	13.83

The deposition modes, designations of the samples under study, and the elemental composition of the samples are presented in Table 1.

The morphology and elemental composition of the coatings were investigated by means of an FEI Quanta 400 FEG scanning electron microscope (SEM) with a built-in energy-dispersive analyzer (Genesis 4000 energy-dispersive X-ray spectroscopy analysis system with an S-UTW-Si(Li) detector) operating at a high residual pressure (10^{-5} Pa). SEM-image analysis, as well as determination of the linear sizes of the components (grains) included in the coatings, was performed via the linear-intercept method with the help of the Adobe Photoshop CS3 software package.

X-ray investigations were carried out using a Bruker D8 Advance diffractometer (CuK_α radiation with $\lambda = 0.15418$ nm) in the Bragg–Brentano geometry. All coatings were studied under the same conditions, namely, the X-ray tube mode where the voltage and current are, respectively, 40 kV and 20 mA; the angles 2θ are 4°–100°; the scanning step is 0.02°; and the exposure time is 6 s.

To analyze the phase composition of the coatings, the PDF-4 database of the International Center for Diffraction Data (ICDD) was employed. The volume fractions of different phases and coating-lattice parameters were calculated according to diffraction-peak characteristics by means of the Powder Cell 2.4 program and the inorganic crystal structure database (ICSD). The crystallite sizes were determined using the Scherrer formula [29]:

$$D_{hkl} = n\lambda/\beta\cos\theta, \quad (1)$$

where D_{hkl} are the crystallite sizes in the directions perpendicular to the (*hkl*) planes, n is the coefficient as a factor of the particle shape (its value is unity), λ is the X-ray wavelength, and β is the experimental diffraction-peak width at half-maximum (in radians). The relative crystal-lattice strain values were calculated on the basis of equation [30]:

$$\Delta d/d = \beta/4\tan\theta, \quad (2)$$

where $\Delta d/d$ are the relative lattice microstrains in the direction perpendicular to the (*hkl*) plane.

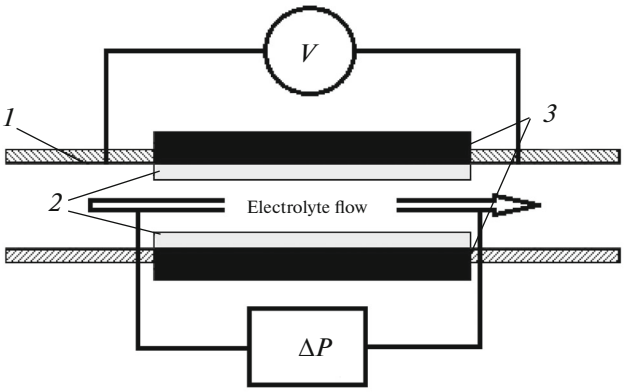

Fig. 1. Block diagram of streaming-potential (current) measurements: *1* are the electrodes, *2* are the samples covered with TiON, *3* are the sample holders, and ΔP is the pressure difference between channel ends.

The coating surface roughness was estimated from the parameters R_a of vertical profile irregularities with the help of a Taylor–Hobson (UK) Talysurf 5–120 measuring system. The quantity R_a was found as the arithmetic mean deviation of the profile over the 1.5-mm reference length according to GOST 2789-73.

The electric potential and electric charge density of the surface of the deposited coatings were measured by an electrical device capable of recording the electric fields of weakly charged bodies [8]. This device is based on the improved Eguchi technique (lifting electrode method) [31]. The charge induced in the measuring electrode located on the coating surface makes it possible to calculate the surface potential V_L [32]:

$$V_L = ((C_{\text{in}} + C_l)/C_l)V_{\text{in}}, \quad (3)$$

where C_l is the air capacitance between the sample surface and the measuring electrode, C_{in} is the input capacitance of an electrometer-type voltmeter, and V_{in} is the potential induced in the measuring electrode. The device's linear resolution determined by the measuring-electrode diameter is 5 mm, and the measurable potentials vary from tens of millivolts to hundreds of volts. The insulation resistance of the device input is no less than 10^{16} Ω, and the input capacitance is less than 5 pF, satisfying the requirements to electric-field measurements in air (GOST 25209–82).

The ζ potential is coupled with the electrokinetic charge density and defined by the interaction between the solution and the coating. The ζ potential of a macroscopic surface is experimentally found from the measured streaming potentials (currents). In this case, the pressure difference is applied parallel to the coating surface (tangential mode). The tangential streaming current is measured in a relatively wide slit channel formed by two identical opposite surfaces. In electrokinetic theory, it is assumed that a cell with opaque channel walls is used to measure the current and/or streaming potential. Then, if the channel height h_{ch} is much greater than the Debye length, the known relationship between the streaming current I_s and the ζ potential is written as [33]

$$I_s = -((Wh_{\text{ch}}\varepsilon_0\varepsilon_r\Delta P)/\eta L)\zeta, \quad (4)$$

where W, L, and h_{ch} are, respectively, the width, length, and height of the channel of the measuring cell; ε_r and η are, respectively, the permittivity and dynamic viscosity of the electrolyte solution; and ΔP is the pressure difference between the channel ends.

A block diagram of the measuring cell is depicted in Fig. 1. Two samples were attached to opposite surfaces of an adjustable gap in the SurPASS analyzer cell. KCl solution with an initial concentration of 1 mM/L served as an electrolyte. The electrolyte's pH value was varied from 5 to 9 by adding an aqueous KOH solution (0.1 mol/L). Before measurements, the solution traveled through the channel for a rather long time (as a rule, 15 min), to attain the equilibrium sample state. The maximum pressure difference was 400 mbar. In the used ranges of pressure and cell sizes, the electrolyte-solution stream was laminar. Measurements demonstrated that the electrolyte-stream velocity linearly depends on the hydrostatic-pressure difference and is described by the Hagen–Poiseuille formula [34]. The streaming potential and current were measured by means of Ag/AgCl electrodes. To reduce the electrode polarization, the stream direction was periodically changed. The equipment was described in detail in [35].

The prepared coatings were dissolved in vitro under conditions similar to an aseptic inflammation, which arises usually after implantation and is accompanied by the congestion of biological fluids in surrounding tissues. The samples were kept in the fluid simulating the composition of the inorganic part of human blood plasma, namely, simulated body fluid (SBF), for 5 weeks. The initial solvent composition corresponded to that of SBF suggested by T. Kokubo et al. [36].

Under sterile conditions, the sample was inserted into a hermetically sealed plastic tube with SBF and cultivated in a thermostat at 37°C. In compliance with ISO 10993-5 recommendations, the solvent volume was chosen to be 4 mL because the sample surface area was 2 cm^2. In the verification procedure, the solvent was (SBF) not in contact with the samples.

At the end of each week of cultivation, fresh solution replaced the old. In the selected samples, the pH value, including the overall value related to organic and inorganic ions, and the concentrations of biologically active sodium, potassium, and calcium ions and a phosphate ion (PO_4^{3-}) were determined using a Konelab 60i (USA) chemical analyzer and Thermo Fisher Scientific (USA) sets. At time intervals of 3 to 5 weeks the samples were taken out of tubes and dried at 120°C for 1 h to record the mass and physical properties of the coatings. The sample masses were weighed using a

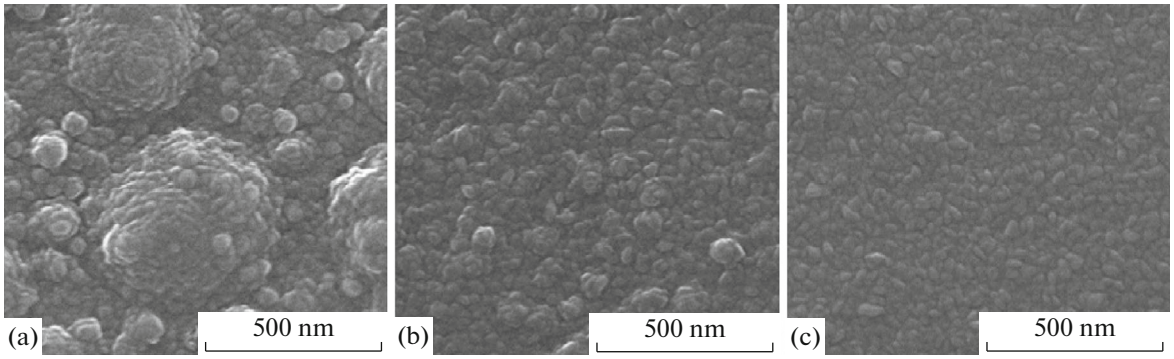

Fig. 2. SEM images of the sample surfaces: (a) TiO_2 (I), (b) TiON (II), and (c) TiON (III).

GR 202 analytical balance with first-grade accuracy according to GOST 24104-201 (upon weighing, the root-mean-square (rms) deviation was 0.023–0.047 mg). The concentrations of dissolved iron ions were calculated from volt–ampere characteristics [37]. The obtained data were processed via mathematical statistics.

RESULTS AND DISCUSSION

The structure and topography of the coating surfaces are important parameters governing cell adhesion. They exhibit columnar structures under applied deposition conditions [38]. The SEM images (Fig. 2) indicate that the coating surfaces have rather complex reliefs and, moreover, are homogeneous without visible defects (cracks, pores, and craters). The coating-structure components are clusters involving small and identically shaped particles whose sizes are on the order of several tens of nanometers or more, namely, agglomerates composed of dome-like fragments (grains). Individual grains possess a fine structure and consist of subnanocrystalline columnar components (substructures) with sizes of several nanometers, which are perpendicular to the substrate–film interface.

The grain parameters were quantitatively estimated by analyzing the grain-size distribution [39]. It was established that, in the case of sample group I (Fig. 2a), the fragment-size distribution corresponds to two scale levels, i.e., is bimodal with maxima at 47 and 280 nm (in the ranges of 14–134 and 134–374 nm, respectively). The average grain size is 115 nm. For sample group II (Fig. 2b), the distribution is also bimodal with maxima at 30 and 70 nm. The maxima conforming to 70 nm is one-seventh that observed at 30 nm. The average grain size is 31 nm. In the case of sample group III (Fig. 2c), the distribution behaves unimodally, and the average particle (grain) size is 28 nm.

Thus, the aforementioned data demonstrate that the increased partial pressure of nitrogen included in the reactive gas leads to a change in the size-distribution function of coating-structure components, namely, the distribution behavior varies from bimodal (sample group I) to unimodal (sample group III), as is shown in Figs. 2a and 2c, respectively. A rise in the partial pressure of nitrogen stimulates the disintegration of the coating's structural components so that their size decreases from 115 (sample group I) to 28 nm (sample group III). With increasing partial pressure of nitrogen, the spherical shape of the coating-structure components, which corresponds to sample group I (Fig. 2a) converts to the rod-like or rice-like shape inherent to sample group III (Fig. 2c). Data on the elemental composition of coatings grown under different conditions, which were obtained from energy-dispersive analysis, are summarized in Table 1.

Figure 3a presents the diffraction patterns of TiO_2- and TiON-covered samples, which comprise the reflections inherent to two modifications of titanium dioxide (anatase and rutile) and peaks corresponding to the α-Fe phase with a body-centered cubic lattice and pertaining to the substrate material.

As was revealed from analysis of the diffraction patterns of the samples with TiO_2 and TiON coatings, the higher nitrogen content alters the diffraction-reflection intensity (Fig. 3b). Most probably, this is caused by a change in the phase composition of the coatings. It was ascertained that, in the case where the coating's nitrogen concentration is no more than 5.71 at %, the volume fractions of anatase and rutile are, respectively, ~60 and only ~30 at % (Table 2). However, when the coating's oxygen content reaches 6.16 at %, the volume fraction of anatase sharply decreases to ~22 at % and, conversely, the volume fraction of rutile increases to ~68 at %.

Along with changes in the phase composition, it was established that the reflection width of the sample coating with 6.16 at % of nitrogen corresponding to the rutile and anatase phases is several angular degrees (Fig. 3b), i.e., considerably exceeds the α-Fe-phase reflection width. There are two reasons for such X-ray line blurring: small (less than 100 nm) sizes of coherent-scattering regions (CSRs) and crystal-lattice microdistortions [40]. For the anatase and rutile

Table 2. Phase compositions, crystal-lattice parameters, average CSR sizes D, and the microstrains of the samples covered with TiO_2 and TiON layers. Data were calculated with the help of the Powder Cell 2.4 program

Coating	Lattice parameters, nm		Volume fraction of phase, %		$\Delta d/d$		D, nm	
	Anatase	Rutile	Anatase	Rutile	Anatase	Rutile	Anatase	Rutile
TiO (I)	$a = 0.38020$ $c = 0.95485$	$a = 0.45982$ $c = 0.30065$	60	38	0.0065	0.0061	15	15
TiON (II)	$a = 0.37883$ $c = 0.95627$	$a = 0.45837$ $c = 0.29565$	58	38	0.0067	0.0061	10	9
TiON (III)	$a = 0.37578$ $c = 0.96790$	$a = 0.45990$ $c = 0.29401$	22	68	0.0062	0.0058	9	8

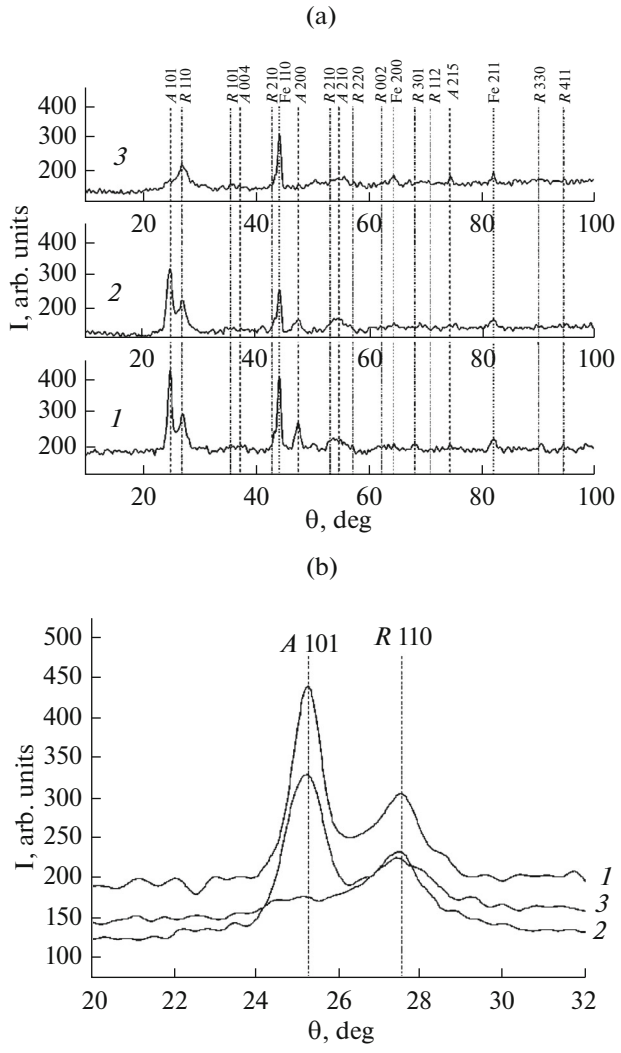

Fig. 3. (a) Diffraction patterns of TiO_2- and TiON-covered samples with different nitrogen contents and (b) variations in the intensity of diffraction peaks: (*1*) TiO_2 (I), (*2*) TiON (II), and (*3*) TiON (III). Here, *A*, *R*, and Fe designate anatase, rutile, and iron, respectively.

phases of the samples with TiON coatings and different nitrogen concentrations, the measured values of CSR sizes and microstrains of the first kind ($\Delta d/d$) are listed in Table 2, from which it follows that both rutile and anatase phases are characterized by small CSR sizes ($D \le 15$ nm) in titanium-oxide coatings (there is no nitrogen in the coating composition of sample group I). After its introduction into the coatings (sample groups II and III), the CSR sizes decreases to $D \le 8$ nm.

The calculated lattice constants of crystalline phases demonstrated that the parameters a and c of the anatase phase decrease and increase, respectively, with increasing nitrogen concentration in the coating. At the same time, the rutile phase exhibits the contrary behavior, namely, a decrease in lattice parameter c is observed (Table 2). The given change in the parameters is probably due to the fact that nitrogen is incorporated into rutile and anatase lattices.

Thus, although the nitrogen concentration increases both in the reactive-gas atmosphere and in the coating, the basic crystalline phase of the coating is titanium dioxide in the form of anatase and rutile. However, nitrogen embedding into the gas-mixture composition leads to a large change in the coating structure, induces variations in the crystal-lattice parameters, and affects the ratio between the crystalline-phase components of the coating and, consequently, CSR sizes.

The electric potential and roughness of the TiO_2 and TiON coatings were measured by means of the technique described above. The roughness R_a of the formed coatings corresponds to classes 12a and 11c if the substrate roughness belongs to class 12b. When the hemocompatibility of a coating is determined, a high roughness class is a positive characteristic. The roughness, thickness, and electric potential of the TiO_2 and TiON coatings, which were obtained at different partial pressures of oxygen and nitrogen, are presented in Table 3. According to the presented data, all prepared TiO_2 and TiON coatings possess surfaces with a negative electric potential. The electric charge of the investigated coatings is evidence that magnetron-discharge

Table 3. Thicknesses L, ζ potentials, roughnesses R_a, electric potentials V, and the contact angles of wettability by water and glycerol (θ_w and θ_g, respectively) of TiO_2 and TiON coatings

Sample		TiO_2 (I)	TiON (II)	TiON (III)
L, nm		192.7 ± 0.09	175.9 ± 0.12	187.0 ± 0.20
pH (IEP)		5.3	6.1	–
ζ, mV (pH 7)		–51	–21	–48
R_a, nm		28.0	25.8	29.5
V, mV		–538 ± 30	–806 ± 40	–836 ± 40
Contact angle	Sample	L316 substrate	TiON (II)	TiON (III)
	θ_w, degree	73.7 ± 1.80	105.7 ± 0.9	112.1 ± 1.8
	θ_g, degree	69.0 ± 4.70	98.8 ± 3.3	95.8 ± 10.4

plasma deposition provides dielectric coatings with electric properties. In all likelihood, the synthesized coatings are "technological components" [41]. On account of sample immersion into a solution, it can be expected that the medium pH greatly affects the sign and amount of charge on the obtained coating surfaces classified as amphoteric oxide layers.

It is evident that negative surface charge conforms to the requirements imposed on hemocompatible coatings. This can be attributed to the fact that such a charge weakens the adhesion of blood cells with a negative ζ potential to the coatings under study. Moreover, the negative surface charge determines the active behavior between the surface and the liquid part of blood.

Measurements of the water (θ_w) and glycerol (θ_g) contact angles indicate (Table 3) that all formed coatings are hydrophobic. Three competitive processes govern the interaction of a surface with a solution: negative surface charges are neutralized because oppositely charged ions are adsorbed, decreasing the electrokinetic potential; similarly charged ions approach a hydrophobic surface, leading to an increase in the electrokinetic potential; and diffuse double layers are compressed due to the higher volume concentration of an electrolyte, which decreases the electrokinetic potential. The degree of the participation of each process occurring on the surface determines the dependence between the electrokinetic potential and the electrolyte composition.

Figure 4 illustrates variations in the ζ potential of the oxide coating and oxynitride coatings with different compositions versus the medium pH at a temperature of $T = 293$ K. The curves shown in Fig. 4 demonstrate that only sample groups II and III have positive and negative ζ potentials at a pH lower and greater than six, respectively. For all synthesized types of coatings (Fig. 4), their values reduce steadily from +20 to –70 mV as the pH grows from 5 to 9. The ζ potential of the majority of coatings is negative. In the case of two types of them prepared in the medium with pH < 6.25, this quantity is positive. For sample groups I and II, its value reaches zero if the pH is, respectively, 5.3 and 6.1 (Table 3). These points can be considered isoelectric points (IEPs). The ζ potential of all types of coatings is negative at pH 7.

The experimentally observed dependence can be interpreted using the Gouy–Chapman–Stern model [42]. From the very beginning, negative charge arises on the coating surface with the formed chemisorbed aqueous layer. The positive surface potential can be caused by its protonation and cation adsorption. At a high pH level, several factors lead to a negative value of the ζ potential. First of all, this is related to the fact that Cl^- and OH^- anions are adsorbed from the solution.

As was mentioned above, it is expected that the pH of the environment will have an appreciable influence on the surface charge of the obtained coatings falling into the class of amphoteric oxides. Indeed, when the samples under study are immersed into an electrolyte (KCl solution), a double electric layer is generated at the boundary with the surface. The thickness thereof depends on the interaction between ions and the surface and specifies the ζ potential. In the vicinity of pH 7 which is physiological for blood, all samples possess negatively charged surfaces (Fig. 4, Table 3).

It should be noted that the ζ potential varies differently depending on the substrate material used. In the case of oxides and titanium oxynitrides, the negative surface charge is neutralized due to potassium-ion deposition and protonation, as was stated above. Chlorine anions and hydroxyl groups are adsorbed on the initially neutral electroconducting steel surface. As a result, the ζ potential becomes negative and increases upon an alkaline shift in the solution pH (Fig. 4). In the primary state, certain steel surface regions can be positively charged because an oxide film contains positively charged ions of iron and alloying metals (chromium and nickel). This can be explained by the insufficient hemocompatibility of medical steel [43].

Table 4. Iron-ion concentration in the SBF and changes in the sample mass Δm after dissolution over 5 weeks

Sample	Dissolution weeks			
	1	3	5	5
	Total iron concentration in the SBF, mg/L			Δm, g
Solvent (control)	0.48 ± 0.2			
L316 substrate	1.13 ± 0.10	2.37 ± 0.30	1.21 ± 0.20	0.11 ± 0.02
TiO_2 (I)	1.14 ± 0.10	0.80 ± 0.20	2.62 ± 0.40	0.10 ± 0.02
TiON (II)	1.45 ± 0.20	0.85 ± 0.20	2.26 ± 0.40	0.04 ± 0.01
TiON (III)	0.63 ± 0.20	1.90 ± 0.20	2.13 ± 0.50	0.02 ± 0.01

Figure 4 is evidence that the values and signs of the ζ potential of all samples are rather close to each other (in the range from +20 to –70 mV) after their contact with the electrolyte. This enables us to suppose that, not only proteins [44], but also water molecules and electrolyte ions regulate the electrokinetic properties of implant surfaces by forming a double electric layer capable of controlling the interaction between the implant and biological systems. Moreover, the metal corrosion rate, as well as the diffusion of doping-element ions being toxic for living systems into the environment [45], is determined by the double electric layer located at the interphase boundary. However, stainless steel is assumed to be a biotolerant material. Coatings based on nitrides and metal oxynitrides have good prospects for application as the anticorrosive protective coatings of implants and endoprostheses [46].

In the context of the foregoing discussion, it was necessary to perform experiments on studying the physical-chemical characteristics of coatings as a function of their dissolution in the SBF. Dissolution data are presented in Table 4. Quantitative chemical analysis indicates a two- to fivefold increase in the iron-ion transition from the coating-free steel substrate into the solution over the entire dissolution time. At the beginning of the third week of dissolution, the iron content of the solution is eight times greater than its maximum permissible concentration in water (0.3 mg/L). In the case of TiO_2 (group I) and TiON (group II, 1/1) coatings, the degree of metal corrosion was appreciably reduced to the control value (from the statistical viewpoint) before the third week of dissolution. The TiON (group III, 1/3) coating improves the corrosion stability as well. Thus, the deposited coatings substantially reduce the stainless-steel corrosion rate, thereby decreasing the risk of metallose around stents after their implantation into blood-vessel lumens. However, the protective effect of coatings is of a short-term character, i.e., with time (in our experiment, by the fifth week of dissolution), coatings can be dissolved so that the substrate becomes uncovered due to ion processes proceeding in the double electric layer at the surface–SBF interface.

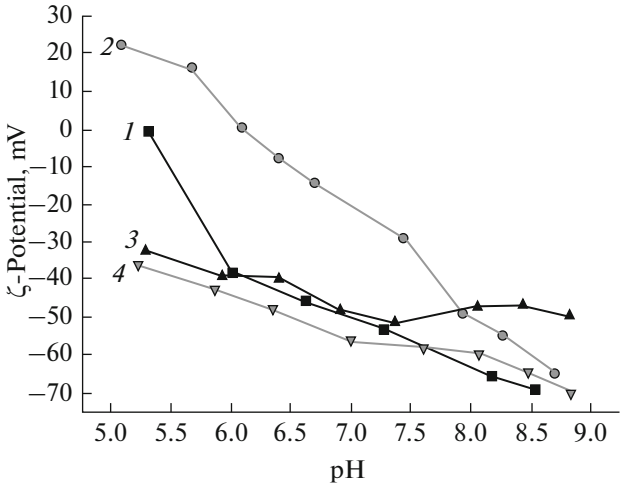

Fig. 4. Dependences between the ζ potential of titanium oxide and oxynitride coatings and the pH value at the temperature $T = 293$ K: (*1*) TiO_2 (I), (*2*) TiON (II), (*3*) TiON (III), and (*4*) coating-free steel substrate.

After the dissolution procedure, the samples were weighed. As a result, a statistically significant increase in their mass was revealed (Table 4). This can be associated with the fact that ions are precipitated from the SBF on the sample surfaces. Coating-free samples, as well as those with oxide coatings, demonstrated the largest increase. On account of the TiON coatings, solution-component precipitation on the samples decreased by a factor of 2.5–5.0.

The question arises as to what is the type of salts that grows on the sample surface in the SBF. First of all, this is concerned with calcium precipitations because implant calcification is extremely undesirable upon contact with blood [47]. In this context, the elemental composition of the solvent (SBF) was further investigated in the dynamics of 5-week interaction with the sample. In addition, special interest must be devoted to potassium (to interpret the ζ-potential measurement results), sodium having the maximum concentration in biological liquids, and inorganic phosphorus as the source of the potential mineraliza-

Table 5. Ion concentrations (mM) in the SBF solution and pH values after 2-week contact with the steel samples covered with TiO_2 or TiON layers

Group	K^+	Na^+	pH	Ca^{2+}	Ca (total)	PO_4^{3-}
SBF (control)	5.46 ± 0.05	151.8 ± 1.6	7.07 ± 0.06	2.28 ± 0.12	2.39 ± 0.06	0.93 ± 0.01
Steel substrate	5.38 ± 0.08	149.4 ± 1.0	7.10 ± 0.03	2.25 ± 0.04	2.39 ± 0.02	0.93 ± 0.02
TiO_2 (I)	5.32 ± 0.04	148.8 ± 0.8	7.08 ± 0.02	2.22 ± 0.04	2.42 ± 0.02	0.93 ± 0.01
TiON (II)	5.42 ± 0.04	150.4 ± 1.8	7.10 ± 0.02	2.28 ± 0.03	2.45 ± 0.02	0.93 ± 0.01
TiON (III)	5.40 ± 0.02	149.8 ± 0.8	7.10 ± 0.02	2.25 ± 0.03	2.45 ± 0.03	0.93 ± 0.01

Table 6. Electrostatic potentials V and water contact angles θ_w of TiO_2 and TiON coatings after 5-week incubation in the SBF

Coating type	V, mV		θ_w, degree	
	before dissolution	after SBF	before dissolution	after SBF
Steel	0 ± 2	244 ± 16	73.7 ± 1.8	48.2 ± 3.1
TiO_2 (I)	−540 ± 30	17 ± 2	90.0 ± 3.0	39.8 ± 3.5
TiON (II)	−810 ± 40	16 ± 2	105.7 ± 0.9	33.4 ± 2.2
TiON (III)	−840 ± 40	−49 ± 3	112.0 ± 2.0	43.3 ± 4.5

tion and ossification of implantation zones (in combination with calcium).

It should be emphasized that the chemical (reference) composition of the initial SBF solution had no statistically significant changes during the entire period of observation (Table 5). This confirms that the chosen electrolyte is stable (i.e., an ionic composition is dynamically balanced) if an irritant is lacking.

The samples under test were kept in a solution for 5 weeks. As a result, it was established that the weekly determined SBF composition remained practically invariable. Under the condition of contact with the tested samples, certain decreases in sodium and, to a lesser extent, potassium (for the TiO_2 coating) ion contents (in the former case, up to 2–3 mM) were found only after the second week of the experiment (Table 5). It is clear that, in the interaction with the SBF (Table 4), the sample masses increase due to ion deposition from the solution onto the surface. It is pertinent to note that the calcium- and phosphorus-ion contents of the solution remained unchanged. This is evidence that their role is insignificant during ion exchange with sample surfaces.

The SEM image of the sample surface without a coating, which was obtained upon keeping in the SBF for 5 weeks (Fig. 5a), indicates that crystals (probably NaCl) are generated within 15–18% of the observation region. For samples with coatings, the crystallization area is 7–11%. When the nitrogen content of the reactive atmosphere reaches 75% (sample group III, $p(O_2)/p(N_2) = 1/3$), small crystals are formed on the coating (Fig. 5c). In this case, large crystals are lacking.

According to the data of the energy-dispersive X-ray spectroscopy of TiON coatings (sample group III, $p(O_2)/p(N_2) = 1/3$), their surface contains coating elements (Ti, O, and N), as well as Na and Cl, after 5-week dissolution in the SBF. This confirms that NaCl crystals grow on the surface. Traces of other coating elements (K, Mg, and Ca), which are included in the SBF, are not observed in the energy-dispersive spectra (see, e.g., Fig. 6). Thus, univalent-ion deposition from the SBF dominates over coating dissolution. Such

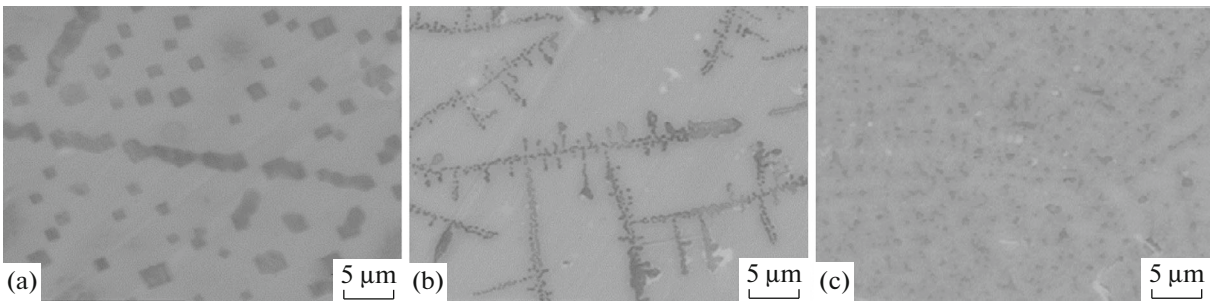

Fig. 5. SEM images of the surface of (a) steel, (b) TiO_2 (I), and (c) TiON (III) after 5-week dissolution in SBF (black crystals are inverted images).

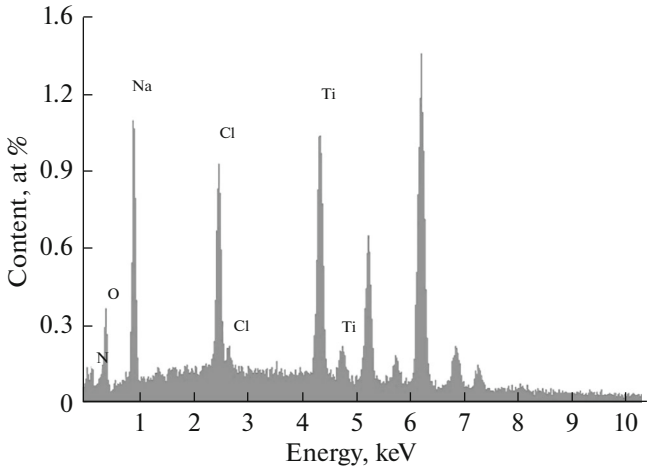

Fig. 6. Energy-dispersive spectrum of the TiON (III) coating after 5-week dissolution in SBF.

dominance explains an increase in the sample mass (Table 4).

In compliance with data obtained from energy-dispersive analysis of the elemental composition of the coatings, traces of calcium are lacking (Fig. 6). This is a positive aspect because the probability that thrombi are generated and the functional properties of stents are lost is decreased without calcification of the tested coatings.

At the same time, since sample surfaces are mineralized during their storage in SBF, their physicochemical properties affecting bio- and hemocompatibility vary greatly, the surface potential decreases, the surface-charge sign is altered, and the surface wettability varies considerably (Table 6).

From measurements of the water and glycerol contact angles performed in air, it is obvious that all prepared coatings are hydrophobic (Table 6). However, after the samples were kept in the SBF, their surfaces become hydrophilic.

CONCLUSIONS

In conformity with the obtained results, the electrostatic surface potential can be varied by controlling the oxygen and nitrogen contents in the titanium-oxynitride coating. When samples are kept in the simulated body fluid, a double electric layer, which regulates ion exchange between an artificial surface and a solvent under contact with a biological liquid, is formed on their surfaces. This process is accompanied not only by corrosion and coating dissolution but also involves the deposition of sodium and chloride ions and the formation of NaCl crystals on surfaces. The coating prevents the transition of iron ions into the solution during the first and second weeks of dissolution, thereby reducing the risk of metallose around the stents after their implantation into blood-vessel lumens and inhibiting the surface calcification process.

According to physical-chemical characteristics and electrokinetic surface properties, TiON coatings are biocompatible and require further studies, including the ascertainment of relations between the electrostatic and electrokinetic potentials. This can stimulate the development of a technique by which the coating behavior is predicted upon contact with blood components.

ACKNOWLEDGMENTS

We are grateful to professors M. Epple and M. Ulbricht for their assistance in experiments and candidate of physics and mathematics M.G. Ostapenko for her help in discussion of the diffraction patterns.

This work was carried out in part at the University of Duisburg-Essen (Germany) and supported by the German Academic Exchange Service (DAAD) (L. Euler grant).

REFERENCES

1. P. K. Chu, J. Y. Chen, L. P. Wang, and N. Huang, Mater. Sci. Eng. Rep. **36**, 143 (2002).
2. N. Huang, Y. X. Leng, P. Yang, J. Y. Chen, H. Sun, J. Wang, G. J. Wan, A. S. Zhao, P. D. Ding, Nucl. Instrum. Methods Phys. Res., Sect. B **242**, 18 (2006).
3. G. Mania, M. D. Feldmanb, D. Patelb, and C. M. Agrawal, Biomaterials **28**, 1689 (2007).
4. M.-H. Chan and F.-H. Lu, Surf. Coat. Technol. **203**, 614 (2008).
5. A. Trenczek-Zajac, M. Radecka, K. Zakrzewska, et al., J. Power Sources **194**, 93 (2009).
6. A. A. Barybin, A. V. Zav'yalov, and V. I. Shapovalov, Glass Phys. Chem. **38**, 396 (2012).
7. R. J. Koerner, L. A. Butterworth, I. V. Mayer, R. Dasbach, and H. J. Busscher, Biomaterials **23**, 2835 (2002).
8. E. S. M. Bahnson, N. Koo, N. Cantu-Medellin, A. Y. Tsui, G. E. Havelka, et al., Nitric Oxide **44**, 8 (2015).
9. K. Ostrikov, E. C. Neyts, and M. Meyyappan, Adv. Phys. **62**, 113 (2013).
10. N. N. Nikitenkov, E. S. Kiselyova, M. E. Konischev, et al., J. Surf. Invest.: X-ray, Synchrotron Neutron Tech. **8**, 1230 (2014).
11. R. Wild, T. Gerling, R. Bussiahn, K. -D. Weltmann, and L. Stollenwerk, J. Phys. D: Appl. Phys. **47**, 5 (2014).
12. C. Werner, H. Korber, R. Zimmermann, S. Dukhin, and H. J. Jacobasch, J. Colloid Interface Sci. **208**, 329 (1998).
13. A. Szymczyk, Y. I. Dirir, M. Picot, I. Nicolas, and F. Barriere, J. Membr. Sci. **429**, 44 (2013).
14. H. Xie, T. Saito, and M. A. Hickner, Langmuir **27**, 4721 (2011).

15. Z. Adamczyk, M. Zaucha, and M. Zembala, Langmuir **26**, 9368 (2010).
16. K. Cai, M. Frant, J. Bossert, G. Hildebrand, K. Liefeith, and K. D. Jandt, Colloids Surf. B **50**, 1 (2006).
17. M. J. Ariza and J. Benavente, J. Membr. Sci. **190**, 119 (2001).
18. A. Yaroshchuk and Th. Luxbacher, Langmuir **26**, 10882 (2010).
19. A. Paar, "Determination of zeta potential of macroscopic solid surfaces using the SurPASS System," http://www.azom.com/article.aspx?ArticleID=5497#filter.
20. C. Werner, U. Konig, A. Augsburg, C. Arnhold, H. Korber, R. Zimmermann, and H.-J. Jacobasch, Colloids Surf. A **159**, 519 (1999).
21. I. O. Smith, M. J. Baumann, and L. R. McCabe, J. Biomed. Mater. Res. **70**, 436 (2004).
22. S. Sundelacruz, M. Levin, and D. L. Kaplan, Stem Cell Rev. **5**, 231 (2009).
23. E. S. Thian, Z. Ahmad, J. Huang, M. J. Edirisinghe, S. N. Jayasinghe, D. C. Ireland, R. A. Brooks, N. Rushton, W. Bonfield, and S. M. Best, Acta Biomater. **6**, 750 (2010).
24. M. Mosseri, I. Tamari, M. Plich, Y. Hasin, et al., Cardiovasc. Revasc. Med. **6**, 2 (2005).
25. P. P. Karjalainen, F. Biancari, A. Ylitalo, L. Raeber, et al., J. Invasive Cardiol. **22**, 322 (2010).
26. S. Windecker, M. Billinger, and O. M. Hess, EuroIntervention **2**, 146 (2006).
27. E. N. Kudryavtseva, V. F. Pichugin, N. N. Nikitenkov, et al., J. Surf. Invest.: X-ray, Synchrotron Neutron Tech. **6**, 688 (2012)
28. NIST Atomic Spectra Database, http://physics.nist.gov/.
29. B. D. Cullity and S. R. Stock, *Elements of X-ray Diffraction* (Prentice Hall, Upper Saddle River, 2001).
30. D. Balzar, N. Audebrand, M. R. Daymond, A. Fitch, A. Hewat, et al., J. Appl. Crystallogr. **37**, 911 (2004).
31. M. Eguchi, Philos. Mag. **49**, 178 (1925).
32. E. A. Gostishchev, R. A. Surmenev, I. A. Khlusov, and V. F. Pichugin, Izv. Tomsk. Politekh. Univ. **319** (2), 108 (2011).
33. C. Werner, H. Körber, R. Zimmermann, S. Dukhin, and H. J. Jacobasch, J. Colloid Interface Sci. **208**, 329 (1998).
34. C. Schaschke, *Fluid Mechanics: Worked Examples for Engineers* (Inst. Chem. Eng., Rugby, 2005).
35. www.paar.ru/catalog_8.html; http://www.anton-paar.com/.
36. S. V. Dorozhkin, E. I. Dorozhkina, and M. Epple, Cryst. Growth Des. **4**, 389 (2004).
37. I. A. Khlusov, G. B. Slepchenko, G. T. Dambaev, et al., *Trace Elements and Nanoparticles* (Nova Science, New York, 2011).
38. M. E. Konischev, O. S. Kuzmin, A. A. Pustovalova, et al., Russ. Phys. J. **56**, 1144 (2014).
39. G. V. Arysheva, N. M. Ivanova, A. A. Pustovalova, and M. E. Konishchev, Adv. Mater. Res. **1085**, 134 (2015).
40. R. S. Vemuri, M. Noor-A-Alam, S. K. Gullapalli, et al., Thin Solid Films **520**, 1446 (2011).
41. V. N. Kestelman, L. S. Pinchuk, and V. A. Goldade, *Electrets in Engineering: Fundamentals and Applications* (Springer, New York, 2000).
42. G. D. Panagiotou, Th. Petsi, K. Bourikas, Ch. S. Garoufalis, et al., Adv. Colloid Interface Sci. **142**, 20 (2008).
43. *Vascular and Intraorgan Stenting: Manual*, Ed. by L. S. Kokov (Graal', Moscow, 2003) [in Russian].
44. K. Cai, M. Frant, J. Bossert, G. Hildebrand, K. Liefeith, and K. D. Jandt, Colloids Surf. B **50**, 1 (2006).
45. N. Hallab, K. Merritt, and J. J. Jacobs, J. Bone Jt. Surg., Am. Vol. **83**, 428 (2001).
46. R. Hubler, A. Cozza, T. L. Marcondes, R. B. Souza, and F. F. Fiori, Surf. Coat. Technol. **1078**, 142 (2001).
47. B. D. Ratner, A. S. Hoffman, F. J. Schoen, and J. E. Lemons, *Biomaterials Science: An Introduction to Materials in Medicine* (Elsevier, London, 2004).

Translated by S. Rodikov